

## High Aspect Ratio Plasmonic Nanotrench Structures with Large Active Surface Area for Label-Free Mid-Infrared Molecular Absorption Sensing

Shkondin, Evgeniy; Repän, Taavi; Panah, Mohammad Esmail Aryaee; Lavrinenko, Andrei; Takayama, Osamu

*Published in:*  
ACS Applied Nano Materials

*Link to article, DOI:*  
[10.1021/acsnm.7b00381](https://doi.org/10.1021/acsnm.7b00381)

*Publication date:*  
2018

*Document Version*  
Peer reviewed version

[Link back to DTU Orbit](#)

*Citation (APA):*  
Shkondin, E., Repän, T., Panah, M. E. A., Lavrinenko, A. V., & Takayama, O. (2018). High Aspect Ratio Plasmonic Nanotrench Structures with Large Active Surface Area for Label-Free Mid-Infrared Molecular Absorption Sensing. *ACS Applied Nano Materials*, 1(3), 1212-1218. DOI: 10.1021/acsnm.7b00381

## DTU Library

Technical Information Center of Denmark

---

### General rights

Copyright and moral rights for the publications made accessible in the public portal are retained by the authors and/or other copyright owners and it is a condition of accessing publications that users recognise and abide by the legal requirements associated with these rights.

- Users may download and print one copy of any publication from the public portal for the purpose of private study or research.
- You may not further distribute the material or use it for any profit-making activity or commercial gain
- You may freely distribute the URL identifying the publication in the public portal

If you believe that this document breaches copyright please contact us providing details, and we will remove access to the work immediately and investigate your claim.



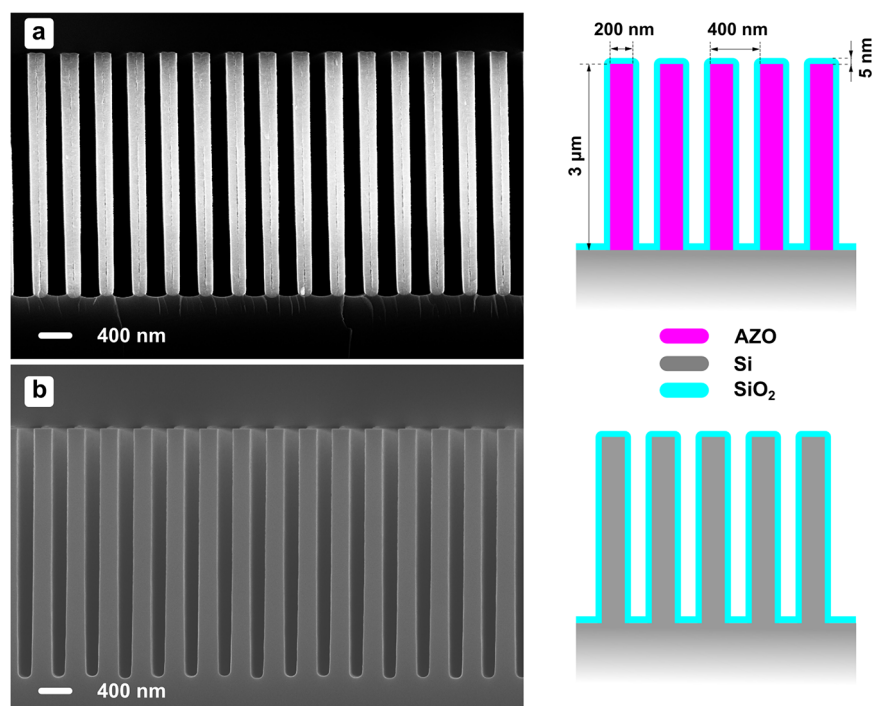


**Figure 1.** Cross-sectional SEM images of (a) fabricated AZO-based HMM structures and (b) Si trenches, as well as corresponding schematic illustrations of AZO and Si trenches with 5 nm thick SiO<sub>2</sub> (not visible in SEM images), respectively.

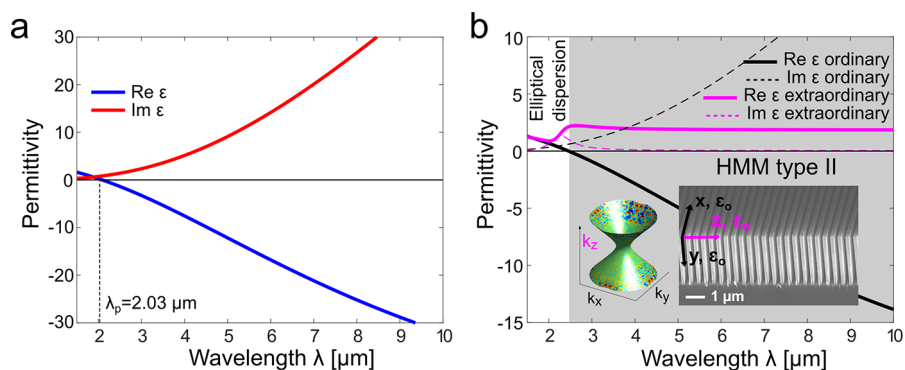


**Figure 2.** (a) Permittivity of AZO thin film in the mid-IR range. (b) Ordinary and extraordinary permittivities of the AZO HMM trench structure based on the EMA approach. The inset shows the cross-sectional, bird-eye view SEM image of the actual AZO HMM, with permittivities shown by the axis. The structure supports the hyperbolic regime from the wavelength above 2.7 μm.

and improve photon–matter interactions. Certain progress is reported with sensing schemes exhibiting sensitivity toward individual molecules. The schemes typically involve in-plane<sup>1,23–34</sup> and vertical pillar plasmonic nanoantennas.<sup>35,36</sup> In these studies, vertical pillars of indium tin oxide (ITO) with protein as an analyte<sup>35</sup> and porous Au coated by 3 nm thick SiO<sub>2</sub> as an analyte<sup>36</sup> exhibit absorption of several percent, in which pillars act as a plasmonic monopole antenna that supports plasmonic modes. Furthermore, a graphene metasurface with voltage tuning was demonstrated.<sup>37</sup> Thanks to the advent of commercially available quantum cascade lasers (QCLs) that are tunable and able to cover a broad wavelength range in the mid-IR, on-chip chemo-biosensors based on principles of vibrational spectroscopy may become feasible.<sup>2,38</sup> In parallel, mid-IR photonics based on the Si platform is also emerging.<sup>17,18,39</sup>

Here we propose the use of hyperbolic metamaterials (HMMs) based on aluminum-doped zinc oxide (AZO) trench

structures as a platform for boosting absorption of mid-IR light by molecules in the trenches as illustrated in Figure 1a. AZO exhibits the plasmonic response (that is a negative real part of the permittivity) in the near- and mid-IR wavelength regions between 1.8 and 3.5 μm depending on doping and fabrication schemes.<sup>40–42</sup> Its permittivity can be widely tuned by doping from near-IR to mid-IR.<sup>40–42</sup> AZO can be deposited by the atomic layer deposition (ALD) technique,<sup>43</sup> allowing a conformal and uniform coating of deep trenches. For demonstration of the potential of the trench HMMs for sensing, we coat the trench structure with a 5 nm thick SiO<sub>2</sub> layer emulating the presence of an analyte. The SiO<sub>2</sub> layer represents a monolayer of proteins, because as was shown in numerous studies of proteins, they typically have thicknesses from 2 to 8 nm.<sup>1,32,44</sup> An amorphous SiO<sub>2</sub> film deposited by ALD has a phonon absorption at around 8.07 μm (1239 cm<sup>-1</sup>),<sup>36,45</sup> which is away from the typical absorption bands of water molecules and, therefore, offers itself as a good model

analyte.<sup>36</sup> We demonstrate over 9% increase in absorption of mid-IR light by the SiO<sub>2</sub> layer. To the best of our knowledge, this is the first report on mid-IR absorption spectroscopy based on nanotrench HMM structures.

## EXPERIMENTAL SECTION

**Fabrication of AZO trench HMMs and deposition of 5 nm SiO<sub>2</sub> layer.** Two types of samples were fabricated: AZO/Air trench structures and Si trench structures with and without 5 nm of ALD deposited SiO<sub>2</sub> (see Figure 1). The structures are grown on the Si substrate. These two types of trenches are the result of one fabrication flow. The full description of the fabrication procedure including deep UV lithography, deep reactive ion etching (DRIE), and atomic layer deposition (ALD) is reported elsewhere.<sup>42</sup> Both structures have trenches of 2.7 μm height and 200 nm wide with a period of  $\Lambda = 0.4$  μm providing effective anisotropy in the long wavelength regime. The ordinary and extraordinary permittivities of the HMM are depicted in Figure 2b, as well as the permittivity of the 100 nm AZO film in Figure 2a. The ordinary permittivity is relevant for electric fields in the plane of the individual trenches, while the extraordinary permittivity is relevant for fields orthogonal to this plane.

Extreme anisotropy of the HMMs with the ability to support propagation of waves with high wavevectors leads to a wide variety of potential applications such as broadband enhancement in the spontaneous emission for a single photon source, subwavelength imaging, and thermal engineering.<sup>46,47</sup> HMMs composed of plasmonic nanopillars<sup>48</sup> and planar multilayer structures<sup>49</sup> have been shown to achieve extremely high sensitivity toward refractive index variations for biosensing on visible to near-infrared wavelengths. Moreover, the HMMs also support unique directional surface waves, named Dyakonov plasmons.<sup>42,50,51</sup>

Conventional deep-UV lithography was used to define grating patterns on standard silicon (100) wafers. DRIE was implemented with a standard Bosch process<sup>52</sup> in order to fabricate a Si template with the 3 μm-deep trenches. An inherent consequence of the Bosch process is the formation of sidewalls roughness known as scallops. They are formed as a result of switching between etching and passivation steps. In this work, the process was fine-tuned in order to reduce this effect by minimizing the switching times and lowering the temperature.<sup>42</sup> Indeed, the resulting Si trench as depicted in Figure 1b has a very smooth sidewall surface suitable for subsequent ALD deposition. Fabricated Si templates were carefully investigated using SEM cross-sectional analysis. Afterward, the processed structures were cleaned in N<sub>2</sub>/O<sub>2</sub> plasma in order to get rid of resist remainings and other organic contaminants. Then, the silicon templates were ALD coated by AZO (using trimethylaluminum, diethylzinc, and water as precursors), until the gratings voids were filled entirely. For the final step, the AZO filling needs to be isolated, and for that purpose, the samples were subjected to Ar<sup>+</sup> sputtering for removal of the ALD deposited top AZO layer opening the silicon trenches. This procedure allows us to etch silicon in-between cavities fully coated with AZO, resulting in the AZO/Air trenches as shown in Figure 1a. In other words, the fabricated AZO trenches are the negative replica of the initial DRIE-prepared Si template. Such AZO structures act as an HMM in the mid-IR wavelength range. The detailed description of the fabrication method for different structures, AZO trenches,<sup>42</sup> AZO pillars,<sup>41</sup> TiN-based trenches,<sup>53</sup> and dielectric trenches,<sup>54</sup> can be found elsewhere.

Finally, the initial Si trench template and AZO/Air HMM trench structures were ALD coated with 5 nm SiO<sub>2</sub>. ALD deposition of silica is based on two precursors—Si[N(C<sub>2</sub>H<sub>5</sub>)<sub>2</sub>]<sub>2</sub> (SAM.24), supplied from AirLiquide<sup>55,56</sup>) as the source of silicon, and O<sub>2</sub> plasma as the oxidation agent, being carried at 300 °C. In order to find the deposition rate, deposition of SiO<sub>2</sub> with thicknesses up to 50 nm on flat and structured Si has been proven prior to deposition on the trench samples. The linear growth conditions were verified by spectroscopic ellipsometry and SEM cross-sectional analysis. It was found that growth of SiO<sub>2</sub> was 0.06 nm/cycle, and therefore, 85 cycles were selected for deposition of a 5 nm thin film on the Si and AZO/Air

HMMs. Such thicknesses are hard to see using cross-sectional SEM measurements, but ellipsometry and X-ray photoelectron spectroscopy (XPS) performed on AZO coated flat dummy wafers confirmed deposition of a thin silica layer with the 5 nm thickness.

**FTIR free-space reflection measurement.** Free-space reflection measurements were conducted by the FTIR spectrometer (VERTEX 70, Bruker). The measurements were performed with the TM-polarized incident light in the wavelength range of  $\lambda = 6.25$ – $10.0$  μm (1600–1000 cm<sup>-1</sup>) with resolution of 2 cm<sup>-1</sup>. Two different samples, AZO and Si trench structures with and without 5 nm thick SiO<sub>2</sub> layers, were used for each measurement. The presented reflectance is the average of 32 scans. For the reference spectrum, TM reflectance from an aluminum mirror at the angle of incidence  $\phi = 12^\circ$  was taken. A wire grid polarizer is used to obtain the TM polarization with the magnetic field in the  $x$ - $z$  plane as shown in the inset of Figure 2b. The incident beam has angular variation of  $\Delta\phi = \pm 1.7^\circ$ . The incident angles were varied in the range  $\phi = 12$ – $50^\circ$  with  $3^\circ$  steps.

## RESULTS AND DISCUSSION

Hyperbolic metamaterials are artificially designed structures that possess unusual indefinite dispersion in a certain region of frequencies.<sup>57</sup> Defining the dispersion relation through wavevector  $\mathbf{k}$ , the isofrequency contour obeys the dispersion equation:

$$\frac{k_x^2 + k_y^2}{\epsilon_o} + \frac{k_z^2}{\epsilon_e} = \frac{\omega^2}{c^2} \quad (1)$$

For naturally occurring materials the ordinary ( $\epsilon_o$ ) and extraordinary ( $\epsilon_e$ ) permittivity components are typically positive, resulting in spherical dispersion in the case of equal permittivities (isotropic materials) or elliptical dispersion when slightly different positive components represent uniaxial materials. The different situation happens when one of the permittivity components becomes negative; in this case, the isofrequency contour has the hyperbolic shape supporting propagation of abnormally high- $k$  waves. There are limited cases when such phenomena are encountered in natural materials,<sup>58</sup> but they all suffer from high losses and narrow bandwidths. Therefore, such structures need to be artificially designed. Two types of geometries are proposed and realized: metal-dielectric multilayers<sup>59</sup> and metallic wires in a dielectric host.<sup>48,60</sup> The case where  $\epsilon_o > 0$  and  $\epsilon_e < 0$  describes a 2-fold hyperboloid and refers to a so-called type-I HMM. It is common for a wire medium and will not be considered here. The opposite scenario,  $\epsilon_o < 0$  and  $\epsilon_e > 0$ , with one-fold symmetry (type-II HMM) mainly represents multilayer structures. Expressions for the ordinary and extraordinary permittivities can be derived within the effective medium approximation (EMA),<sup>60</sup> under the condition that the thicknesses of individual layers are deeply subwavelength:

$$\epsilon_o = f_m \cdot \epsilon_m + f_d \cdot \epsilon_d \quad (2)$$

$$\epsilon_e = \frac{\epsilon_m \cdot \epsilon_d}{f_d \cdot \epsilon_m + f_m \cdot \epsilon_d} \quad (3)$$

where  $\epsilon_m$  and  $\epsilon_d$  are the permittivities of metal and dielectric, and  $f_m, f_d$  are the corresponding fractions of metal and dielectric in the multilayer. The trench structure we fabricated is an example of a multilayer with vertically arranged layers. The period of trenches ( $\Lambda = 0.4$  μm) is deeply subwavelength for the mid-IR wavelength range  $\lambda = 6.25$ – $10$  μm (1600–1000 cm<sup>-1</sup>,  $\Lambda/\lambda = 1/17.5$ – $1/25$ ), allowing application of the effective media theory and subsequent introduction of the

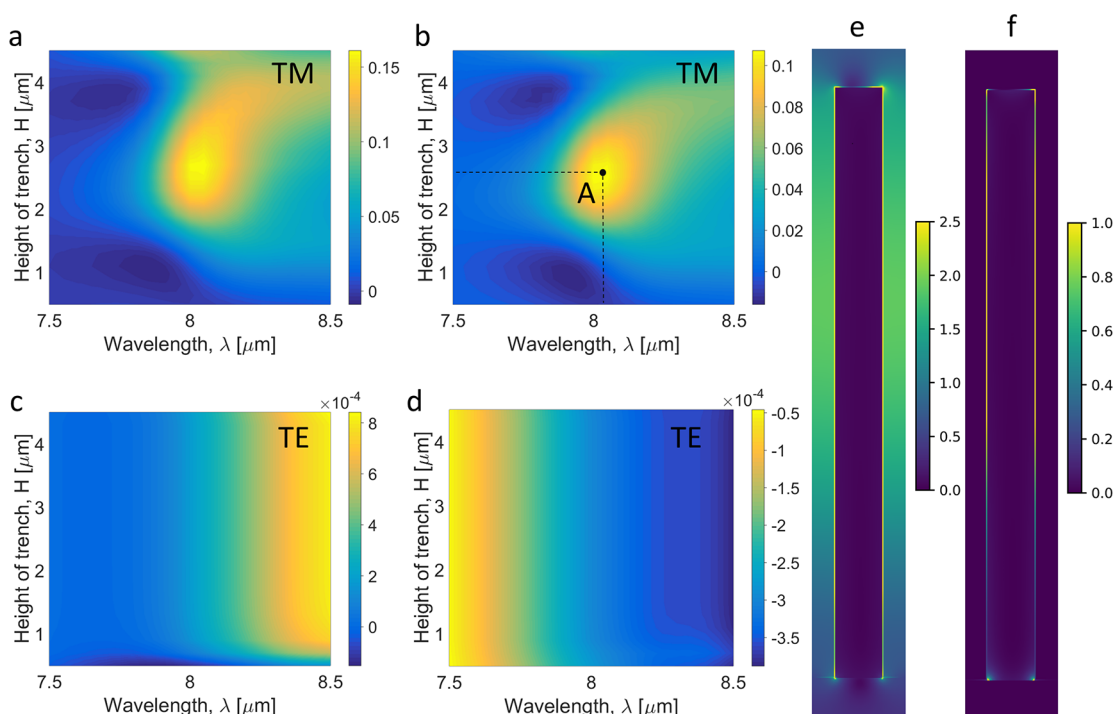


**Figure 3.** Simulated reflection difference between AZO trench structures with and without the 5 nm thick SiO<sub>2</sub> layer in terms of wavelengths and heights of trenches,  $H$ . (a) With the imaginary part of the AZO's permittivity reduced by 10 times and (b) the actual permittivity of AZO for TM-polarized incident light. (c), (d) Same as (a) and (b) for TE-polarized light. (e) Field profile. The color bar is normalized by incident field. (f) Absorption. The color bar has arbitrary units. The angle of incidence is 12°.

effective parameters. Our AZO/Air trench structure has a zero crossing wavelength for  $\epsilon_o$  around 2.7  $\mu\text{m}$  and becomes Type II HMMs ( $\epsilon_o < 0$  and  $\epsilon_e > 0$ )<sup>42</sup> within an extremely wide band; see Figure 2b. Theoretically our AZO trench HMM supports bulk plasmon modes at 3  $\mu\text{m}$  and above in a wide wavelength range.<sup>42</sup> Wavelengths longer than 3  $\mu\text{m}$  cover most of the absorption bands of interesting/biologically relevant molecules.<sup>3</sup> Moreover, most of the important absorption resonances in the biomedical sensing are ranged between 2.5 and 10  $\mu\text{m}$  (4000 to 1000  $\text{cm}^{-1}$ ).<sup>6</sup>

**Numerical simulation.** The differences in reflection of two samples, field profiles, and absorption in Figure 3 were calculated by the Comsol Multiphysics software package. The permittivities of AZO, Si, and SiO<sub>2</sub> were taken from refs 41, 42, and 45, respectively. The simulations were conducted for both TE- and TM-polarized light with the angle of incidence 12° counted from the optical axis as shown in the inset of Figure 2b. Figures 3a and 3b show the simulated reflection difference between the samples with and without the 5 nm SiO<sub>2</sub> layer with reduced and realistic losses of AZO, respectively. The absorption of the real structure drops to approximately 0.1 (10%) from the reduced loss case of 0.15 (15%). This suggests that a material with lower absorption, such as a doped semiconductor,<sup>61</sup> can improve the absorption. From Figure 3, the optimum height of the trenches is 2.5 to 2.7  $\mu\text{m}$  in both cases. Therefore, we choose the trench height to be 2.7  $\mu\text{m}$ , providing almost optimum absorption around 8  $\mu\text{m}$  in wavelength. In a different sensing situation, where targeted analytes exhibit absorption for different wavelengths, the structural parameters, especially the height of the trenches, should be optimized to operate effectively at certain wavelengths. Figure 3e shows the electric field profile in a trench. We can see the presence of a strong field between the AZO

trenches, indicating the feature of a bulk plasmon that propagates in the bulk of the structure.<sup>51</sup> Figure 3f shows enhanced absorption in trenches, stemming from the interaction between the bulk plasmons and analyte. According to Figure 3e, there are hot spots at the four edges of the trenches, and corresponding absorption at these places is high (Figure 3f). However, from the color bar in Figure 3e, the hot spots have the field enhancement factor of 2–3, which are not so significant, and they occupy relatively small volumes of the entire trenches. Therefore, most of absorption originates from the middle of the trenches as shown in Figure 3f. This also suggests that the analyte should be preferably located between the trenches rather than on the top or bottom close to the hot spots for enhanced absorption. In general this structure would be very suitable for “gas” sensing when analyte molecules are equally located inside the trenches rather than located on the top or bottom of the trenches. There are mainly two mechanisms of absorption enhancement: (1) Extended surface area of the trench structures—ca. 14.5 times more surface area in the trench structure relative to a flat surface with the same footprint. (2) The HMM structures support bulk plasmon modes in the trenches which bounce between the top and bottom interfaces of the trenches, interacting with the analyte and resulting in higher absorption in comparison with the surface waves case.

In contrast with the TM-polarized incident light, the TE-polarized light sees the structure as a metal since the electric field is oscillating along the trenches ( $x$ -axis in the inset of Figure 2b), experiencing  $\epsilon_o < 0$ . Hence, incident light is reflected from the structure and does not propagate inside the trenches, resulting in weak interaction with the SiO<sub>2</sub> analyte layer.

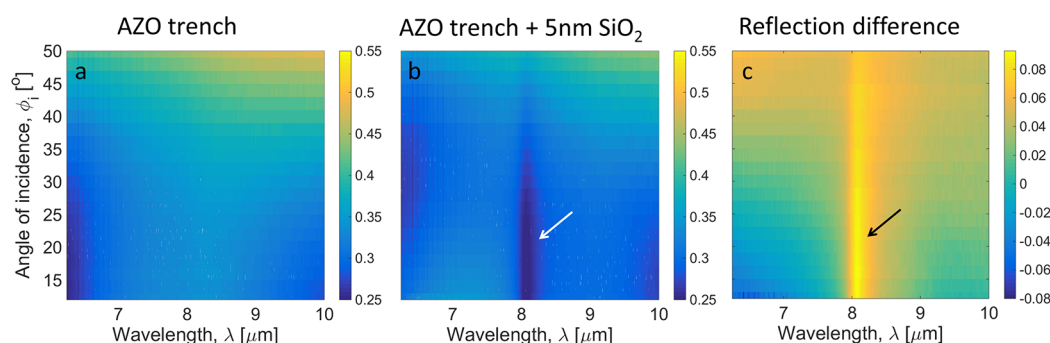


**Figure 4.** Absorption spectra. Measured free-space reflection of AZO trench HMM structures (a) without and (b) with a 5 nm thick SiO<sub>2</sub> layer. (c) Reflection difference for  $\phi = 12^\circ - 50^\circ$  with TM-polarized incidence light. The absorption associated with the SiO<sub>2</sub> layer is indicated by an arrow.

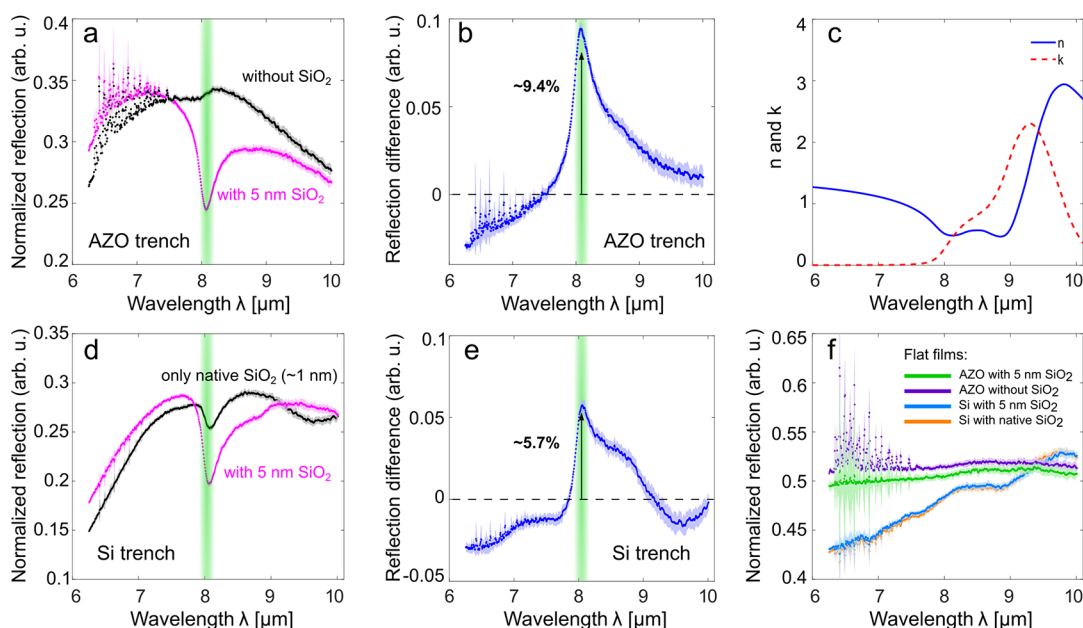


**Figure 5.** Absorption enhancement. (a) Measured free-space reflection of AZO trench structures with (dotted pink) and without (dotted black) the 5 nm thick SiO<sub>2</sub> layer. (b) Reflection difference. (c) Real ( $n$ ) and imaginary part ( $k$ ) of the refractive index of SiO<sub>2</sub> from ref 45. (d) Measured reflection of Si trench structures with (dotted pink) and without (dotted black) the 5 nm thick SiO<sub>2</sub> layer. (e) Reflection difference. (f) Reflection from the 100 nm AZO film on the Si substrate with and without the 5 nm SiO<sub>2</sub> film, as well as from the Si substrate with and without the 5 nm SiO<sub>2</sub> film. Note that Si trenches and substrates have a few nanometers of a native oxide layer. The angle of incidence is  $\phi = 12^\circ$  with TM-polarized incidence light for all reflection measurements. Colored shade represents an error bar.

Figure 4a,b shows the measured reflectance for the samples with and without 5 nm thick SiO<sub>2</sub> analyte layers. There is a reflection dip associated with the phonon absorption of the SiO<sub>2</sub> stretching that appears around 8.07  $\mu\text{m}$  (Figure 4b). In order to highlight the absorption enhancement, Figure 4c presents the reflection difference of both samples, giving the absorption equivalent of SiO<sub>2</sub> layers. The reflection difference is the highest at the lowest angle of incidence,  $\phi = 12^\circ$ , reaching 0.09 (9%). Figure 5a and b shows the reflectance spectra and their difference at  $\phi = 12^\circ$ . The real and imaginary part of SiO<sub>2</sub>'s refractive index is shown in Figure 5c for reference. Note that multiple reflection dips below 7.5  $\mu\text{m}$  are caused by the water absorption. We assume that absorption from the SiO<sub>2</sub> film follows the Beer–Lambert law, exhibiting the saturation of absorption as the thickness increases.<sup>62</sup> The AZO trench structures exhibit a high reflection difference of approximately 9.4%, which shows qualitatively good agreement with the prediction of Figure 3.

In order to clarify the contribution of enlarged surface area and bulk plasmon modes, we also characterize reflection from a

Si trench structure, a 100 nm AZO film on the flat Si substrate, and the flat Si substrate with and without conducted 5 nm SiO<sub>2</sub> layers. The 5 nm SiO<sub>2</sub> films on the flat AZO and Si surface do not give detectable absorption around  $\lambda = 8 \mu\text{m}$  [Figure 5f]. Figure 5d and 5e show the measured reflection and its difference of the Si trench structures, resulting in 5.7% difference. Since the Si trenches are dielectric, they do not support any bulk plasmon mode. We deduce that this absorption is caused by the enlarged surface area of the trench structure. Therefore, the rest of  $9.4 - 5.7\% = 3.7\%$  is the contribution of the bulk plasmon modes, resulting in more than 50% enhancement of absorption over the surface effect.

## CONCLUSIONS

In conclusion, we demonstrate the enhancement of absorption by a 5 nm thick SiO<sub>2</sub> layer in the mid-IR wavelength range of 6.25–10  $\mu\text{m}$  (1600–1000  $\text{cm}^{-1}$ ). The enhancement originates from nanostructuring of large active surfaces with plasmonic trenches, and as shown it can be used for effective molecular

sensing. The structures are composed of multiple high-aspect ratio (1:6.7) subwavelength AZO trenches on a Si substrate, providing 14.5 times more surface area for residing of analyte molecules than the flat surface. The fabrication process for the trench structures is fully compatible with the large-scale CMOS technology. Moreover, the doping level of AZO can be changed to adjust its plasmonic properties for desired wavelengths, leading to the optimum sensitivity of molecules on demand. The AZO trench HMM exhibits broadband performance in the range of wavelengths important for molecular sensing. We report about over 9% absorption increase. This enhancement is enabled by a combination of the extended surface area and the bulk plasmon modes supported by the trench structure. Our demonstration shows that such structures can be effectively designed to detect traces of a target analyte and molecular sensing in mid-IR spectroscopy.

## AUTHOR INFORMATION

### Corresponding Author

\*E-mail: [otak@fotonik.dtu.dk](mailto:otak@fotonik.dtu.dk). Phone: +45 4525 6571. Fax: +45 4593 6581.

### ORCID

Andrei V. Lavrinenko: [0000-0001-8853-2033](https://orcid.org/0000-0001-8853-2033)

Osamu Takayama: [0000-0003-3525-3262](https://orcid.org/0000-0003-3525-3262)

### Author Contributions

E.S. fabricated the samples. T.R. conducted modeling of the structure. O.T. conceived the idea, designed and performed the experiments, and supervised the work. M.E.A.P. and A.V.L. contributed to the discussions of results and manuscript writing. All authors have given approval to the final version of the manuscript.

### Notes

The authors declare no competing financial interest.

## ACKNOWLEDGMENTS

This work was supported by Villum Fonden "DarkSILD project" (11116) and Direktør Ib Henriksens Fond, Denmark. The authors would like to acknowledge the support from the Danish National Center for Micro- and Nanofabrication (DTU Danchip). O.T. sincerely acknowledges Dr. M. D. Stine Munkholm-Larsen, Resident Medical Officer, The Doctors in Gothersgade, Copenhagen K, Denmark, for fruitful discussion and valuable comments on the detection of antibodies and proteins, and clinical diagnoses.

## REFERENCES

- (1) Adato, R.; Aksu, S.; Altug, H. Engineering mid-infrared nanoantennas for surface enhanced infrared absorption spectroscopy. *Mater. Today* **2015**, *18*, 436–446.
- (2) Sieger, M.; Mizaikoff, B. Toward On-Chip Mid-Infrared Sensors. *Anal. Chem.* **2016**, *88*, 5562–5573.
- (3) Haas, J.; Mizaikoff, B. Advances in Mid-Infrared Spectroscopy for Chemical Analysis. *Annu. Rev. Anal. Chem.* **2016**, *9*, 45–68.
- (4) Maltesen, M. J.; Bjerregaard, S.; Hovgaard, L.; Havelund, S.; van de Weert, M.; Grohgan, H. Multivariate analysis of phenol in freeze-dried and spray-dried insulin formulations by NIR and FTIR. *AAPS PharmSciTech* **2011**, *12*, 627–636.
- (5) Sieger, M.; Haas, J.; Jetter, M.; Michler, P.; Godejohann, M.; Mizaikoff, B. Mid-Infrared Spectroscopy Platform Based on GaAs/AlGaAs Thin-Film Waveguides and Quantum Cascade Lasers. *Anal. Chem.* **2016**, *88*, 2558–2562.
- (6) Barth, A. Infrared spectroscopy of proteins. *Biochim. Biophys. Acta, Bioenerg.* **2007**, *1767*, 1073–1101.

(7) Ataka, K.; Kottke, T.; Heberle, J. Thinner, smaller, faster: IR techniques to probe the functionality of biological and biomimetic systems. *Angew. Chem., Int. Ed.* **2010**, *49*, 5416–5424.

(8) Ataka, K.; Stripp, S. T.; Heberle, J. Surface-enhanced infrared absorption spectroscopy (SEIRAS) to probe monolayers of membrane proteins. *Biochim. Biophys. Acta, Biomembr.* **2013**, *1828*, 2283–2293.

(9) Roy, S.; Covert, P. A.; Fitzgerald, W. R.; Hore, D. K. Biomolecular structure at solid-liquid interfaces as revealed by nonlinear optical spectroscopy. *Chem. Rev.* **2014**, *114*, 8388–8415.

(10) López-Lorente, Á. I.; Mizaikoff, B. Mid-infrared spectroscopy for protein analysis: Potential and challenges. *Anal. Bioanal. Chem.* **2016**, *408*, 2875–2889.

(11) Tuzson, B.; Jágerská, J.; Looser, H.; Graf, M.; Felder, F.; Fill, M.; Tappy, L.; Emmenegger, L. Highly Selective Volatile Organic Compounds Breath Analysis Using a Broadly-Tunable Vertical-External-Cavity Surface-Emitting Laser. *Anal. Chem.* **2017**, *89*, 6377–6383.

(12) Shaw, R. A.; Mantsch, H. H. In *Infrared Spectroscopy in Clinical and Diagnostic Analysis (Encyclopedia of Analytical Chemistry)*; Wiley: Hoboken, NJ, 2008.

(13) Kasahara, R.; Kino, S.; Soyama, S.; Matsuura, Y. Noninvasive glucose monitoring using mid-infrared absorption spectroscopy based on a few wavenumbers. *Biomed. Opt. Express* **2018**, *9*, 289–302.

(14) Wang, L.; Mizaikoff, B. Application of multivariate data-analysis techniques to biomedical diagnostics based on mid-infrared spectroscopy. *Anal. Bioanal. Chem.* **2008**, *391*, 1641–1654.

(15) Hansen, L.; De Beer, T.; Pierre, K.; Pastoret, S.; Bonnegarde-Bernard, A.; Daoussi, R.; Vervaet, C.; Remon, J. P. FTIR spectroscopy for the detection and evaluation of live attenuated viruses in freeze dried vaccine formulations. *Biotechnol. Prog.* **2015**, *31*, 1107–1118.

(16) Petrich, W.; Lewandrowski, K. B.; Muhlestein, J. B.; Hammond, M. E. H.; Januzzi, J. L.; Lewandrowski, E. L.; Pearson, R. R.; Dolenko, B.; Früh, J.; Haass, M.; Hirsch, M. M.; Köhler, W.; Mischler, R.; Möcks, J.; Ordóñez-Llanos, J.; Quader, O.; Somorjai, R.; Staib, A.; Sylvén, C.; Werner, G.; Zerback, R. Potential of mid-infrared spectroscopy to aid the triage of patients with acute chest pain. *Analyst* **2009**, *134*, 1092–1098.

(17) Lin, P. T.; Giammarco, J.; Borodinov, N.; Savchak, M.; Singh, V.; Kimerling, L. C.; Tan, D. T. H.; Richardson, K. A.; Luzinov, I.; Agarwal, A. Label-Free Water Sensors Using Hybrid Polymer-Dielectric Mid-Infrared Optical Waveguides. *ACS Appl. Mater. Interfaces* **2015**, *7*, 11189–11194.

(18) Jin, T. N.; Li, L. G.; Zhang, B.; Lin, H. Y. G.; Wang, H. Y.; Lin, P. T. Monolithic Mid-Infrared Integrated Photonics Using Silicon-on-Epitaxial Barium Titanate Thin Films. *ACS Appl. Mater. Interfaces* **2017**, *9*, 21848–21855.

(19) Tütüncü, E.; Kokoric, V.; Wilk, A.; Seichter, F.; Schmid, M.; Hunt, W. E.; Manuel, A. M.; Mirkarimi, P.; Alameda, J. B.; Carter, J. C.; Mizaikoff, B. Fiber-Coupled Substrate-Integrated Hollow Waveguides: An Innovative Approach to Mid-Infrared Remote Gas Sensors. *ACS Sens.* **2017**, *2*, 1287–1293.

(20) Tombez, L.; Zhang, E. J.; Orcutt, J. S.; Kamlapurkar, S.; Green, W. M. J. Methane absorption spectroscopy on a silicon photonic chip. *Optica* **2017**, *4*, 1322–1325.

(21) Schwarz, B.; Reiningger, P.; Ristanić, D.; Detz, H.; Andrews, A. M.; Schrenk, W.; Strasser, G. Monolithically integrated mid-infrared lab-on-a-chip using plasmonics and quantum cascade structures. *Nat. Commun.* **2014**, *5*, 4085.

(22) Adato, R.; Altug, H. In-situ ultra-sensitive infrared absorption spectroscopy of biomolecule interactions in real time with plasmonic nanoantennas. *Nat. Commun.* **2013**, *4*, 1–10.

(23) Neubrech, F.; Pucci, A.; Cornelius, T. W.; Karim, S.; García-Etxarri, A.; Aizpurua, J. Resonant plasmonic and vibrational coupling in a tailored nanoantenna for infrared detection. *Phys. Rev. Lett.* **2008**, *101*, 2–5.

(24) Law, S.; Yu, L.; Rosenberg, A.; Wasserman, D. All-semiconductor plasmonic nanoantennas for infrared sensing. *Nano Lett.* **2013**, *13*, 4569–4574.

- (25) Michel, A. K. U.; Chigrin, D. N.; Maß, T. W. W.; Schönauer, K.; Salinga, M.; Wuttig, M.; Taubner, T. Using low-loss phase-change materials for mid-infrared antenna resonance tuning. *Nano Lett.* **2013**, *13*, 3470–3475.
- (26) Baldassarre, L.; Sakat, E.; Frigerio, J.; Samarelli, A.; Gallacher, K.; Calandrini, E.; Isella, G.; Paul, D. J.; Ortolani, M.; Biagioni, P. Midinfrared Plasmon-Enhanced Spectroscopy with Germanium Antennas on Silicon Substrates. *Nano Lett.* **2015**, *15*, 7225–7231.
- (27) Maß, T. W. W.; Taubner, T. Incident Angle-Tuning of Infrared Antenna Array Resonances for Molecular Sensing. *ACS Photonics* **2015**, *2*, 1498–1504.
- (28) Braun, A.; Maier, S. A. Versatile Direct Laser Writing Lithography Technique for Surface Enhanced Infrared Spectroscopy Sensors. *ACS Sens.* **2016**, *1*, 1155–1162.
- (29) Cerjan, B.; Yang, X.; Nordlander, P.; Halas, N. J. Asymmetric Aluminum Antennas for Self-Calibrating Surface-Enhanced Infrared Absorption Spectroscopy. *ACS Photonics* **2016**, *3*, 354–360.
- (30) Milla, M. J.; Barho, F.; González-Posada, F.; Cerutti, L.; Charlot, B.; Bomers, M.; Neubrech, F.; Tournie, E.; Taliercio, T. Surface-enhanced infrared absorption with Si-doped InAsSb/GaSb nanoantennas. *Opt. Express* **2017**, *25*, 26651–26661.
- (31) Weber, K.; Nesterov, M. L.; Weiss, T.; Scherer, M.; Hentschel, M.; Vogt, J.; Huck, C.; Li, W.; Dressel, M.; Giessen, H.; Neubrech, F. Wavelength Scaling in Antenna-Enhanced Infrared Spectroscopy: Toward the Far-IR and THz Region. *ACS Photonics* **2017**, *4*, 45–51.
- (32) Etezadi, D.; Warner, J. B.; Ruggeri, F. S.; Dietler, G.; Lashuel, H. A.; Altug, H. Nanoplasmonic mid-infrared biosensor for in vitro protein secondary structure detection. *Light: Sci. Appl.* **2017**, *6*, e17029.
- (33) Barho, F. B.; Gonzalez-Posada, F.; Milla, M. J.; Bomers, M.; Cerutti, L.; Tournie, E.; Taliercio, T. Highly doped semiconductor plasmonic nanoantenna arrays for polarization selective broadband surface-enhanced infrared absorption spectroscopy of vanillin. *Nanophotonics* **2018**, *7*, 507–516.
- (34) Weber, K.; Nesterov, M. L.; Weiss, T.; Scherer, M.; Hentschel, M.; Vogt, J.; Huck, C.; Li, W.; Dressel, M.; Giessen, H.; Neubrech, F. Wavelength Scaling in Antenna-Enhanced Infrared Spectroscopy: Toward the Far-IR and THz Region. *ACS Photonics* **2017**, *4*, 45–51.
- (35) Chen, K.; Guo, P.; Dao, T. D.; Li, S. Q.; Ishii, S.; Nagao, T.; Chang, R. P. Protein-Functionalized Indium-Tin Oxide Nanoantenna Arrays for Selective Infrared Biosensing. *Adv. Opt. Mater.* **2017**, 1–5.
- (36) Garoli, D.; Calandrini, E.; Bozzola, A.; Ortolani, M.; Cattarin, S.; Barison, S.; Toma, A.; De Angelis, F. Boosting infrared energy transfer in 3D nanoporous gold antennas. *Nanoscale* **2017**, *9*, 915–922.
- (37) Rodrigo, D.; Limaj, O.; Janner, D.; Etezadi, D.; Abajo, F. J. G. D.; Pruneri, V.; Altug, H. Mid-infrared plasmonic biosensing with graphene. *Science* **2015**, *349*, 165–168.
- (38) Lin, P. T.; Singh, V.; Wang, J.; Lin, H.; Hu, J.; Richardson, K.; Musgraves, J. D.; Luzinov, I.; Hensley, J.; Kimerling, L. C.; Agarwal, A. Si-CMOS compatible materials and devices for mid-IR micro-photonics. *Opt. Mater. Express* **2013**, *3*, 1474–1487.
- (39) Roelkens, G.; Dave, U.; Gassenq, A.; Hattasan, N.; Hu, C.; Kuyken, B.; Leo, F.; Malik, A.; Muneeb, M.; Ryckeboer, E.; Uvin, S.; Hens, Z.; Baets, R.; Shimura, Y.; Gencarelli, F.; Vincent, B.; Loo, R.; Van Campenhout, J.; Cerutti, L.; Rodriguez, J.-B.; Tournie, E.; Chen, X.; Nedeljkovic, M.; Mashanovich, G.; Shen, L.; Healy, N.; Peacock, A. C.; Liu, X.; Osgood, R.; Green, W. Silicon-based heterogeneous photonic integrated circuits for the mid-infrared. *Opt. Mater. Express* **2013**, *3*, 1523–1536.
- (40) Naik, G. V.; Shalae, V. M.; Boltasseva, A. Alternative plasmonic materials: Beyond gold and silver. *Adv. Mater.* **2013**, *25*, 3264–3294.
- (41) Shkondin, E.; Takayama, O.; Panah, M. E. A.; Liu, P.; Larsen, P. V.; Mar, M. D.; Jensen, F.; Lavrinenko, A. V. Large-scale high aspect ratio Al-doped ZnO nanopillars arrays as anisotropic metamaterials. *Opt. Mater. Express* **2017**, *7*, 1606–1627.
- (42) Takayama, O.; Shkondin, E.; Bodganov, A.; Panah, M. E. A.; Golenitskii, K.; Dmitriev, P.; Repän, T.; Malureanu, R.; Belov, P.; Jensen, F.; Lavrinenko, A. V. Midinfrared surface waves on a high aspect ratio nanotrench platform. *ACS Photonics* **2017**, *4*, 2899–2907.
- (43) George, S. M. Atomic Layer Deposition: An Overview. *Chem. Rev.* **2010**, *110*, 111–131.
- (44) Cetin, A. E.; Etezadi, D.; Altug, H. Accessible Nearfields by Nanoantennas on Nanopedestals for Ultrasensitive Vibrational Spectroscopy. *Adv. Opt. Mater.* **2014**, *2*, 866–872.
- (45) Kischkat, J.; Peters, S.; Gruska, B.; Semtsiv, M.; Chashnikova, M.; Klinkmüller, M.; Fedosenko, O.; Machulik, S.; Aleksandrova, A.; Monastyrskiy, G.; Flores, Y.; Masselink, W. T. Mid-infrared optical properties of thin films of aluminum oxide, titanium dioxide, silicon dioxide, aluminum nitride, and silicon nitride. *Appl. Opt.* **2012**, *51*, 6789–6798.
- (46) Guo, Y.; Newman, W.; Cortes, C. L.; Jacob, Z. Applications of hyperbolic metamaterial substrates. *Adv. Optoelectron.* **2012**, *2012*, 1–9.
- (47) Cortes, C. L.; Newman, W.; Molesky, S.; Jacob, Z. Quantum nanophotonics using hyperbolic metamaterials. *J. Opt.* **2012**, *14*, 063001.
- (48) Kabashin, V.; Evans, P.; Pastkovsky, S.; Hendren, W.; Wurtz, G. A.; Atkinson, R.; Pollard, R.; Podolskiy, V. A.; Zayats, A. V. Plasmonic nanorod metamaterials for biosensing. *Nat. Mater.* **2009**, *8*, 867–871.
- (49) Sreekanth, K. V.; Alapan, Y.; ElKabbash, M.; Ilker, E.; Hinczewski, M.; Gurkan, U. A.; De Luca, A.; Strangi, G. Extreme sensitivity biosensing platform based on hyperbolic metamaterials. *Nat. Mater.* **2016**, *15*, 621–627.
- (50) Jacob, Z.; Narimanov, E. E. Optical hyperspace for plasmons: Dyakonov states in metamaterials. *Appl. Phys. Lett.* **2008**, *93*, 221109.
- (51) Takayama, O.; Bogdanov, A.; Lavrinenko, A. V. Photonic surface waves on metamaterial interfaces. *J. Phys.: Condens. Matter* **2017**, *29*, 463001.
- (52) Lindroos, V.; Tilli, M.; Lehto, A.; Motooka, T.; Veijola, T. *Handbook of Silicon Based MEMS Materials and Technologies*; William Andrew Publishing: Norwich, NY, 2010.
- (53) Shkondin, E.; Repän, T.; Takayama, O.; Lavrinenko, A. V. High aspect ratio titanium nitride trench structures as plasmonic biosensor. *Opt. Mater. Express* **2017**, *7*, 4171–4182.
- (54) Shkondin, E.; Takayama, O.; Lindhard, J. M.; Larsen, P. V.; Mar, M. D.; Jensen, F.; Lavrinenko, A. V. Fabrication of high aspect ratio TiO<sub>2</sub> and Al<sub>2</sub>O<sub>3</sub> nanogratings by atomic layer deposition. *J. Vac. Sci. Technol., A* **2016**, *34*, 031605.
- (55) Dussarrat, C. (Air Liquide). Method of forming silicon oxide containing films. WO 2006097525, 2006.
- (56) AirLiquide (<http://www.airliquide.com>).
- (57) Poddubny, A.; Iorsh, I.; Belov, P.; Kivshar, Y. Hyperbolic metamaterials. *Nat. Photonics* **2013**, *7*, 948–957.
- (58) Narimanov, E. E.; Kildishev, A. V. Metamaterials: Naturally hyperbolic. *Nat. Photonics* **2015**, *9*, 214–216.
- (59) Hoffman, A. J.; Alekseyev, L.; Narimanov, E. E.; Gmachl, C.; Sivco, D. L. Negative refraction in mid-infrared semiconductor metamaterials. *Nat. Mater.* **2007**, *6*, 946–950.
- (60) Ferrari, L.; Wu, C.; Lepage, D.; Zhang, X.; Zhaowei, L. Hyperbolic metamaterials and their applications. *Prog. Quantum Electron.* **2015**, *40*, 1–40.
- (61) Aryaee; Panah, M. E.; Takayama, O.; Morozov, S. V.; Kudryavtsev, K. E.; Semenova, E. S.; Lavrinenko, A. V. Highly doped InP as a low loss plasmonic material for mid-IR region. *Opt. Express* **2016**, *24*, 29077–29088.
- (62) Mayerhöfer, T. G.; Mutschke, H.; Popp, J. Employing theories far beyond their limits -The Case of the (Boguer-) Beer-Lambert law. *ChemPhysChem* **2016**, *17*, 1948–1955.